Journal of Neuroscience Methods 277 (2017) 46–55

Contents lists available at ScienceDirect

Journal of Neuroscience Methods

journal homepage: www.elsevier.com/locate/jneumeth

A semi-automated method for rapid detection of ripple events on interictal voltage discharges in the scalp electroencephalogram

Catherine J. Chu[a,*], Arthur Chan[b], Dan Song[a], Kevin J. Staley[a], Steven M. Stufflebeam[c,d], Mark A. Kramer[e]

[a] Department of Neurology, Massachusetts General Hospital, Boston, MA 02114, United States
[b] Voci Technologies, Inc. 6301 Forbes Ave. #120, Pittsburg, PA, 15217, United States
[c] Athinoula A. Martinos Center for Biomedical Imaging, Department of Radiology, Massachusetts General Hospital, Boston, MA 02114, United States
[d] Harvard-MIT Program in Health Sciences and Technology, Institute for Medical Engineering and Science, Massachusetts Institute of Technology, Cambridge, MA 02139, United States
[e] Department of Mathematics and Statistics, Boston University, Boston, MA 02215, United States

HIGHLIGHTS

- Spike-ripple events, in which fast oscillations co-occur with voltage discharges, can be detected automatically in the scalp EEG.
- A combination of multiple quantitative features makes detection of spike-ripple events accurate.
- Rapid, quantitative identification of spike-ripple activity supports clinical application in epilepsy.

ARTICLE INFO

Article history:
Received 7 September 2016
Received in revised form 5 December 2016
Accepted 13 December 2016
Available online 14 December 2016

Keywords:
EEG
High frequency oscillations
Ripples
Automated detection

ABSTRACT

Background: High frequency oscillations are emerging as a clinically important indicator of epileptic networks. However, manual detection of these high frequency oscillations is difficult, time consuming, and subjective, especially in the scalp EEG, thus hindering further clinical exploration and application. Semi-automated detection methods augment manual detection by reducing inspection to a subset of time intervals. We propose a new method to detect high frequency oscillations that co-occur with interictal epileptiform discharges.
New method: The new method proceeds in two steps. The first step identifies candidate time intervals during which high frequency activity is increased. The second step computes a set of seven features for each candidate interval. These features require that the candidate event contain a high frequency oscillation approximately sinusoidal in shape, with at least three cycles, that co-occurs with a large amplitude discharge. Candidate events that satisfy these features are stored for validation through visual analysis.
Results: We evaluate the detector performance in simulation and on ten examples of scalp EEG data, and show that the proposed method successfully detects spike-ripple events, with high positive predictive value, low false positive rate, and high intra-rater reliability.
Comparison with existing method: The proposed method is less sensitive than the existing method of visual inspection, but much faster and much more reliable.
Conclusions: Accurate and rapid detection of high frequency activity increases the clinical viability of this rhythmic biomarker of epilepsy. The proposed spike-ripple detector rapidly identifies candidate spike-ripple events, thus making clinical analysis of prolonged, multielectrode scalp EEG recordings tractable.

1. Introduction

Brief bursts of high frequency oscillations (80–600 Hz) have been implicated as promising biomarkers for epileptic networks (Traub and Jefferys, 1994; Traub et al., 1996; Traub et al., 2001; Bragin et al., 1999; Worrell and Gotman, 2011). Many groups have reported ripple (80–200 Hz) and fast ripple (>200 Hz) activity in

* Correspondence to: 175 Cambridge Street, Ste 340, Boston, MA 02114, United States.
E-mail address: cjchu@mgh.harvard.edu (C.J. Chu).

http://dx.doi.org/10.1016/j.jneumeth.2016.12.009
0165-0270/

human intracranial electrode recordings and have shown that both of these high frequency oscillations localize to the seizure onset zone (Bragin et al., 1999; Worrell et al., 2008; Worrell et al., 2004; Jirsch et al., 2006; Jacobs et al., 2009; Wu et al., 2010), correlate with seizure occurrence (Zijlmans et al., 2009), and with a lower threshold for after-discharges after electrical stimulation (Jacobs et al., 2010). Although activity in the fast ripple frequency band is generated by cortical regions that are too small to generate useful scalp EEG signals (Tao et al., 2007; Andrade-Valenca et al., 2011), ripples have been successfully detected in non-invasive scalp electroencephalogram (EEG) recordings, dramatically increasing the clinical relevance and potential of these biomarkers to include non-surgical patient populations. Ripples have been identified in the scalp EEG from children with electrical status epilepticus of sleep (Kobayashi et al., 2010); epileptic spasms (Kobayashi et al., 2004; Inoue et al., 2008) and focal epilepsy (Andrade-Valenca et al., 2011; Kobayashi et al., 2010; Andrade-Valença et al., 2012; van Klink et al., 2016). Similar to reports from invasive recordings, ripple activity in non-invasive EEG colocalizes with the seizure onset zone (Andrade-Valenca et al., 2011; Andrade-Valença et al., 2012) and correlates with severity of disease (van Klink et al., 2016).

Despite the promise that ripples hold for improved identification, localization, and tracking of the disease course in epilepsy, several challenges have impeded more aggressive application of these biomarkers in clinical epilepsy. First, it is difficult to separate pathologic from non-pathologic high frequency oscillations. Prior studies evaluating high frequency oscillations in scalp EEG have predominantly reported events in the ripple frequency range (Kobayashi et al., 2010; Kobayashi et al., 2004; Inoue et al., 2008; Andrade-Valenca et al., 2011). However, ripples have been observed in both epileptic and non-epileptic cortex (Bragin et al., 1999; Axmacher et al., 2008; Engel et al., 2009; Buzsaki and Lopes da Silva, 2012) and invasive recordings have shown that oscillations in the ripple band may not be as specific for epileptic cortex as fast ripples (>250 Hz; Bragin et al., 1999; Staba et al., 2004; Staba et al., 2007).

Second, identification of high frequency oscillations on scalp EEG is manually laborious, limiting the size of the datasets that can be screened. Because these events are brief (50–150 ms) and have low amplitude, review of 10 min of data from a limited number of electrodes can take an expert reviewer up to 15 h (Jacobs et al., 2009). Although several automated detectors have been developed for intracranial recordings (Zelmann et al., 2012; Blanco et al., 2010; Gardner et al., 2007) non-invasive recordings introduce more artifacts, which result in significantly more false positive events (Von Ellenrieder et al., 2012), thereby limiting the practical application of this tool to smaller datasets. A more selective detector of ripple events would facilitate investigation of larger datasets, enabling a better understanding of how fast oscillations track with and contribute to disease and normal physiology.

Both intracranial and non-invasive recordings have demonstrated that the majority of ripple and fast ripple events in epileptiform cortex co-occur with interictal epileptiform discharges or "spikes" (Urrestarazu et al., 2007; Von Ellenrieder et al., 2012; Jacobs et al., 2009; van Klink et al., 2016). Population based studies have demonstrated that interictal spikes are highly specific for epilepsy, present in only 0.5–2.4% of the general population (Eeg-Olofsson et al., 1971; Bennett, 1967; Gregory et al., 1993). Here we propose to detect the co-occurrence of ripples and spikes in the scalp EEG using a semi-automated spike-ripple detector. This approach leverages the well-characterized signal features of ripples with the specificity of the interictal spike to improve the efficiency of identification and quantification of ripples in non-invasive scalp EEG recordings. We show that the spike-ripple detector performs well in simulations and human non-invasive EEG data from ten patients with benign epilepsy with centrotemporal spikes. Compared to the standard manual detection method, the proposed semi-automated procedure for spike-ripple detection has a high positive predictive value and low false positive rate.

2. Methods

2.1. Implementation of the spike-ripple detector

Implementation of the spike-ripple detector proceeds in two steps. We first provide a qualitative outline of these steps, shown schematically in Fig. 1. We then describe each step in detail. The spike-ripple detector is available for application and further development at https://github.com/Mark-Kramer/Spike-Ripple-Detector-Method. The first step is to identify candidate ripple events by bandpass filtering the data between 100 and 300 Hz (see Step 1 below), computing the amplitude envelope, and finding times where this envelope is large (*i.e.*, times where the envelope is in the top 15% of all envelope values observed in the data) and remains large for more than 20 ms. The second step is to identify candidate spike-ripple events. To do so, we compute six features for each candidate ripple event. These features capture the existing notions of a regular and persistent high frequency oscillation initiating on the ascent of an interictal spike (Zelmann et al., 2009; Zijlmans et al., 2009; Von Ellenrieder et al., 2012; van Klink et al., 2016).

Candidate spike-ripple events are subsequently validated through visual inspection. This visual inspection consists of the following display elements near the candidate spike-ripple event: (1) the unfiltered EEG data, (2) the bandpass filtered data (bandpass 100–300 Hz, see Step 1 below), and (3) the spectrogram. These visualizations are common for the manual detection or validation of ripple events (van Klink et al., 2016; Kobayashi et al., 2010; Bénar et al., 2010; Crépon et al., 2010).

Step 1: Select candidate ripple events. We first bandpass filter the data for the chosen channel. The bandpass filter is an equiripple FIR filter of order 170, with pass-band from 100 to 300 Hz (pass-band ripple 0.1 dB), a frequency of the first stop-band of 60 Hz (stop-band attenuation 80 dB), and a frequency of the second stop-band of 350 Hz (stop-band attenuation 40 dB). We choose the wide (40 Hz) frequency interval between the edges of the first stop-band and first pass-band to reduce the filter order; a lower filter order reduces the impact of artifacts created by sudden, large changes in voltage. The choice of the first stop-band is determined by the frequency of electrical noise (60 Hz). We note that the filter attenuates activity at 80 Hz by only 10 dB, so that events at this frequency pass through the filter with moderate attenuation. We also include frequencies up to 300 Hz in the pass-band; this is consistent with visual inspection of the spike-ripple events, in which the activity is only high-pass filtered (van Klink et al., 2016). We then construct the analytic signal by applying the Hilbert transform to the filtered data, and compute the amplitude envelope. We select an *envelope threshold* as the value of the amplitude envelope greater than a percentage of the amplitude envelope values computed for the entire data set. In this way, the distribution of all observed amplitude envelope values for the channel is used to define the envelope threshold. We show in Results that an envelope threshold of 85% is a reasonable choice. Next, we find all time points at which the amplitude envelope exceeds the envelope threshold; if two of these time points are separated by less than 5 ms, all values between these time points are declared above the envelope threshold. The purpose of this last operation is to increase the robustness of the detections to noisy perturbations during which the amplitude envelope briefly falls below the envelope threshold. Finally, we identify all time intervals of at least 20 ms during which the amplitude envelope exceeds the envelope threshold. These inter-

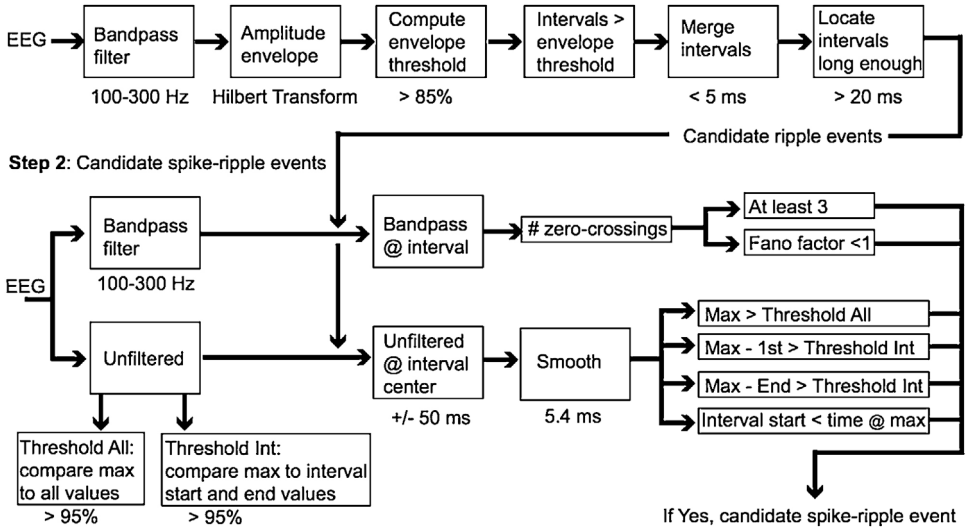

Fig. 1. Diagram of the candidate ripple detection process (Step 1) and the candidate spike-ripple detection process (Step 2). In this figure, each block corresponds to a procedure of the detection process. The passband of the band-pass filters is indicated below the corresponding block. Below the threshold blocks, we indicate the percent threshold. In Step 1, the times below blocks indicate the values used to merge intervals (5 ms) and to locate intervals long enough (>20 ms). In Step 2, the times below blocks indicate the time surrounding the center of the interval (±50 ms) and the duration of smoothing (5.4 ms). Threshold All (box at lower left) is computed using the entire duration (*i.e.*, "all") of unfiltered data. Threshold Int (box at lower right) is computed through a resampling procedure that creates surrogate intervals ("Int") from the entire duration of unfiltered data. The last set of six blocks (narrow rectangles at bottom right) must all be satisfied in Step 2 to declare a candidate spike-ripple event.

vals establish the *candidate ripple events* which are then analyzed in Step 2.

Step 2: Select candidate spike-ripple events. In this step, we apply a series of tests to each candidate ripple event identified in Step 1. Candidate ripple events that pass all of these criteria are labeled *candidate spike-ripple events*, and saved for visual analysis and validation. For each candidate ripple event, we first select the bandpass filtered data (100–300 Hz) at the time of the candidate ripple event. From these filtered data, we identify the times of positive zero-crossings (*i.e.*, where the filtered data transitions from negative to positive) and analyze two quantities. First, we require the number of zero crossings be greater than or equal to three; although no formal definition exists, high frequency oscillations have been characterized as oscillations consisting of at least four cycles (Zelmann et al., 2009; Zijlmans et al., 2009; Von Ellenrieder et al., 2012; van Klink et al., 2016). Here, we choose the less strict inclusion criteria of three cycles. Second, we require that the Fano factor computed using the time intervals between zero-crossing is less than 1. The purpose of computing the Fano factor is to enforce regularity of the bandpass filtered data; when the Fano factor is small (here, less than 1), the time between zero-crossings is more regular than expected for a random (Poisson) process, and therefore more characteristic of a sinusoidal oscillation.

We then select the unfiltered data associated with the candidate ripple event. To do so, we first determine the center time of the interval of the candidate ripple event. We then select unfiltered data that begins 50 ms before this center time, and 50 ms after this center time, resulting in a 100 ms interval of unfiltered data that surrounds the center of the candidate ripple event. We smooth this unfiltered data using a moving average filter of length 5.4 ms and compute four quantities that capture the notion of a ripple co-occurring with an interictal discharge (Von Ellenrieder et al., 2012; van Klink et al., 2016). First, we compute the maximum value of the smoothed data in this interval, and require that this maximum value exceeds 95% of all values from the entire duration of unfiltered data. The purpose of this operation is to identify ripple events that occur within ± 50 ms of a large voltage value consistent with an interictal spike. Second and third, we compute the difference between the maximum value of the smoothed unfiltered data in this interval and the value of the smoothed unfiltered data at the beginning and end of the interval. We require that both of these quantities exceed a threshold value computed through resampling as follows. First, we select a random 50 ms interval from the entire duration of the unfiltered data, and compute the difference between the maximum value and the first value of the unfiltered data within this interval. We then repeat this resampling procedure 10,000 times to create a distribution of these differences, and define as a threshold the 95th percentile. The purpose of this operation is to check that the maximum value in the interval is larger than expected compared to the beginning and end of the interval; we expect this condition to be satisfied during an interictal discharge, before and after which the voltage decrease is large. We note that this resampling, or bootstrapping, procedure provides a powerful method to create this distribution from the data without requiring an explicit model of the distribution (Efron and Gong, 1983). Fourth, we require that the maximum value of the smoothed data occur after the start time of the candidate ripple event. The purpose of this operation is to check that the ripple begins before the peak of the interictal spike.

Candidate ripple events that satisfy all six of these conditions are declared candidate spike-ripple events (Fig. 1). All candidate spike-ripple events are stored for subsequent visual analysis and verification.

2.2. Simulations

To examine detector performance, we simulate four categories of time series. The details to implement each simulation are described below. Within each category, we simulate 100 instances of noisy data, each of duration 10 min with sampling frequency 2035 Hz. We then apply the spike-ripple detector to each instance of the simulated data, and assess detector performance by computing the false detection rate, the positive predictive rate, and the sensitivity. For each simulation category, we report the average of these quantities, and the maximum and minimum values, over the 100 simulated instances.

2.2.1. Simulation: pink noise

Pink noise data were simulated to preserve the relationship $P(f) \sim f^{-0.5}$, where $P(f)$ is the sample power spectral density at frequency f, as observed in neural field activity (He et al., 2010). Additional time series features were added to the pink noise activity created in this way to produce the remaining simulation categories.

2.2.2. Simulation: pink noise with artifacts

We add brief duration (50 ms) triangle pulses to the simulated pink noise data. Compared to the pink noise data, the pulses were larger; the height of each pulse is chosen to be 20 times the standard deviation of the pink noise activity. These pulses provide a simple representation of an artifact known to impact the detection of high frequency oscillations (Kramer et al., 2008; Bénar et al., 2010). For each 10 min simulation, we include pulses periodically at a rate of 1 Hz, corresponding to 600 total pulses. We do not expect the spike-ripple detector to detect these artefactual events.

2.2.3. Simulation: pink noise with spikes

To generate these data, we add spikes of stereotypical shape to the simulated pink noise time series. We define a stereotypical spike as the EEG activity averaged over all spikes manually marked by a board certified clinical neurophysiologist (CJC; N = 188) from Patient E. We scale the stereotypical spike amplitude so that the maximum value of the spike is 20 times the standard deviation of the pink noise activity. We add the stereotypical spikes to the pink noise data at a rate of 1 Hz, which results in 600 spikes during a 10 min simulation. Because the spikes from Patient E lack ripples (see Table 1 in Results), we do not expect to detect these events.

2.2.4. Simulation: pink noise with spike-ripples

To create these data, we add ripple activity to the previous simulation category. The ripple events consist of 50 ms intervals of 110–120 Hz activity, with an approximately Gaussian-shaped envelope. We chose this frequency range as representative of the high frequency oscillations that occur during a ripple, and to capture the notion that ripple activity observed in the scalp EEG exhibits an approximately sinusoidal shape (Von Ellenrieder et al., 2012). To construct the ripple activity, we first filter white noise data between 110 and 120 Hz (finite-impulse response filter with order 100 and zero-phase shift) to create 50 ms of ripple activity. We then multiply these data by a Hanning taper, so that the 50 ms interval of ripple activity begins and ends at 0, and add this ripple activity to the rising phase of a stereotypical spike. In this way, the spike now co-occurs with a ripple. We note that we create a different instance of the ripple (through simulation of a new white noise time series) before adding it to the stereotypical spike. We set the standard deviation of the ripple equal to 1/20 the standard deviation of the stereotypical spike; this choice approximates the observed difference between the large amplitude spike and small amplitude ripple in the EEG data studied here (see next section). We then scale the stereotypical spike amplitude so that the maximum value of the spike is 20 times the standard deviation of the pink noise activity. We consider two scenarios that include spike-ripple events. In the first, we add a ripple to each stereotypical spike, so that 600 spike-ripple events occur in a 10 min simulation. In the second, we add a ripple to every third spike, so that 400 spikes without ripples and 200 spike-ripple events occur in a 10 min simulation. We expect the spike-ripple detector to detect only the spike-ripple events.

2.3. Scalp EEG patient recordings

We consider scalp EEG data recorded from ten patients with benign epilepsy with centrotemporal spikes. Patients' ages ranged from 8.0 to 14.9 years (mean 11.5 years); 7 were male; 6 patients were seizure free for over 1 year (controlled) and 4 patients had active seizures within one year of EEG. EEGs were recorded with a 70-channel electrode cap, based on a geometrically even distribution of electrodes across the scalp (Easycap, Vectorview, Elekta-Neuromag, Helsinki, Finland) with additional electrodes placed at T1 and T2, using a sampling rate of 2035 Hz. Electrooculogram and electrocardiogram recordings were simultaneously obtained to assist with artifact identification. Data were visually inspected by a board certified clinical neurophysiologist (CJC) and large movement, muscle artifacts and electrodes with poor recording quality removed. A minimum of 10 min of artifact-free, non-REM sleep recordings from each patient were used for analysis. For select analysis, 10 min of wake recordings were also analyzed. The research received prior approval by the Massachusetts General Hospital and Boston University institutional review board and informed consent was obtained from each patient.

2.4. Measures of detector performance

We compute four measures of spike-ripple detector performance: positive predictive value (PPV), sensitivity, false positive rate, and the kappa statistic. We briefly define these measures here. The positive predictive value is computed as,

$$\mathrm{PPV} = \mathrm{TP}/(\mathrm{TP} + \mathrm{FP}),$$

where TP is the number of true positive detections and FP is the number of false positive detections. The sensitivity is defined as,

$$\mathrm{Sensitivity} = \mathrm{TP}/(\mathrm{TP} + \mathrm{FN}),$$

where FN is the number of false negatives. We note that, to compute the sensitivity, we must know when true spike-ripple events occur in the data. These true events are known in simulation, or defined as the time of spike-ripple events as determined by an expert reviewer (CJC) through manual inspection of the *in vivo* data.

The false positive rate is defined as the number of false positive spike-ripple detections per second. To assess intra-rater reliability of spike-ripple detections in the *in vivo* data, we compute the kappa statistic,

$$\mathrm{kappa} = (p_o - p_e)/(1 - p_e),$$

where p_o is the relative observed agreement of the rater, and p_e is the hypothetical probability of chance agreement. To compute kappa, the rater is randomly presented twice with each candidate spike-ripple event detected *in vivo*, and asked to validate the occurrence of a ripple through visual inspection, as described in Results.

We note that these measures of detector performance are derived from positive events, and do not require specification of true negatives. True negative events are difficult to define in these data in which event detection is rare and almost all of the recording corresponds to true negatives (Gardner et al., 2007; Von Ellenrieder et al., 2012).

3. Results

Having defined the method of spike-ripple detection (Fig. 1, and Methods), we now apply it to simulated data and clinical EEG recordings from ten patients. We show that the proposed method behaves as expected.

3.1. Simulation results

We consider five simulation scenarios. The purpose of these simulations is to illustrate the behavior of the spike-ripple detection method in idealized scenarios in which the expected behavior of

Table 1
The spike-ripple detector performs well in ten patients. The first column indicates the number of spikes (N) detected by visual inspection at one electrode in each patient. The second column indicates the number of spikes with ripples detected through visual analysis. The third column indicates the number of spike-ripples identified by the proposed detector and validated through visual inspection. The remaining columns indicate the false positive rate (FPR), sensitivity, and positive predictive value (PPV) of the spike-ripple detector compared to visual analysis.

	N	Visual ripples @ spikes	Detector validated (detected)	FPR [Hz]	Sensitivity	PPV
Patient A	234	74	22 (35)	0.022	0.30	0.63
Patient B	133	65	63 (93)	0.050	0.97	0.68
Patient C	14	11	9 (27)	0.030	0.82	0.33
Patient D	103	1	0 (8)	0.013	0	0
Patient E	188	0	0 (16)	0.027	0	0
Patient F	8	0	0 (7)	0.012	0	0
Patient G	0	0	0 (0)	0	0	0
Patient H	0	0	0 (0)	0	0	0
Patient I	0	0	0 (4)	0.007	0	0
Patient J	0	0	0 (0)	0	0	0

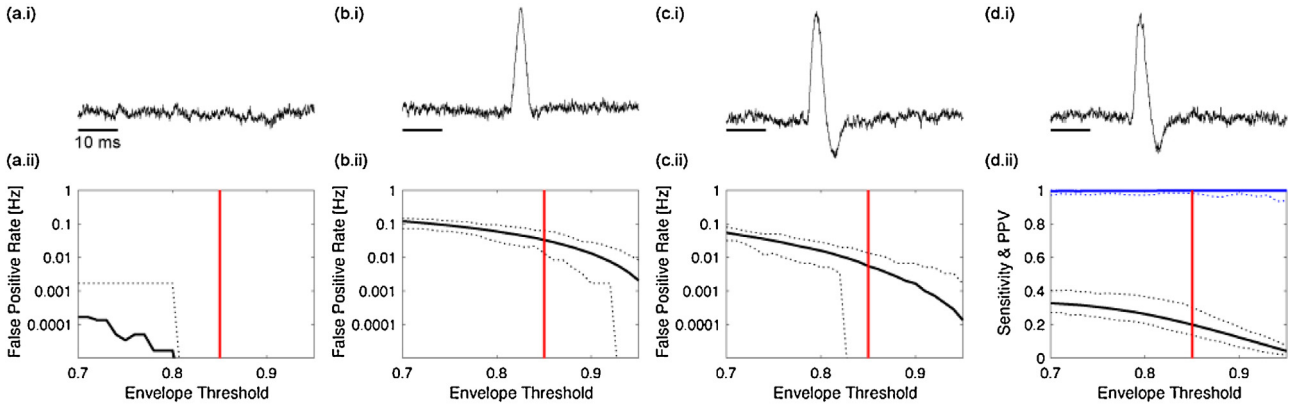

Fig. 2. Examples of spike-ripple detector performance in four simulated scenarios. In (a–c), the simulations lack spike-ripple events. (a) Pink noise simulated data. (b) Pink noise data with sharp artifact. (c) Pink noise with stereotypical spike without ripple. In (d), spike-ripple events occur embedded in pink noise. Panel (i) of each subfigure illustrates an example of the simulated time series events, and panel (ii) shows the false positive rate in (a–c), and the sensitivity (black) and positive predictive value (blue) in (d) versus the envelope threshold. Solid curves indicate the average value over 100 simulations; dotted curves indicate the maximum and minimum values over 100 simulations. The vertical red line denotes an envelope threshold of 0.85. (For interpretation of the references to colour in this figure legend, the reader is referred to the web version of this article.)

the detector is known. As we show below, the spike-ripple detector behaves as expected in each scenario. We begin with the case of simulated pink noise activity (*i.e.*, a random process with power spectrum that decreases with increasing frequency; see example time series in Fig. 2a (i)). We simulate 100 instances of these data, each of duration 10 min (sampling rate 2035 Hz) and apply the spike-ripple detector to each instance while varying a parameter of the detector: the envelope threshold. This parameter controls the number of candidate ripple events determined in Step 1 of the detector. Choosing a small value for this threshold permits more events to reach Step 2 of the detector. We find that this parameter more strongly impacts detector performance than the either the maximum value threshold or the 50 ms interval threshold (*Threshold All* and *Threshold Int* in Fig. 1; not shown). We vary the envelope threshold between values of 0.7 and 0.95, and compute the false positive rate (*i.e.*, the number of false detections per second; see Methods). We show the resulting false positive rate versus the envelope threshold in Fig. 2a (ii). From these data, we find an average false detection rate below 0.001 Hz for all choices of envelope threshold. We conclude that, in this simulation, the false positive rate is small; as expected for these pink noise data – which lack both spikes and ripples – the detector rarely identifies candidate ripple events.

In the second simulation scenario, the data consist of pink noise activity interspersed with sharp artifacts (here, triangle pulses of duration 50 ms) which occur at a rate of 1 Hz. We show an example 1 s interval of these simulated data in Fig. 2b (i); visual inspection reveals the obvious manifestation of the triangle pulse. As in the previous example, we simulate 100 instances of these data, each of duration 10 min (sampling rate 2035 Hz); because the triangle pulses occur at a rate of 1 Hz, there are 600 triangle pulses per instance of data. We apply the spike-ripple detector to these data and find an average false positive rate between 0.1 Hz and 0.001 Hz, depending on the choice of envelope threshold (Fig. 2b (ii)). Although the number of candidate spike-ripple events detected has increased compared to the case of pink noise alone, the false positive rate per second remains low when the envelope threshold is high enough; for example, an envelope threshold of 0.85 produces an average false positive of 0.033 Hz, much lower than the 1 Hz rate of triangle pulse occurrence. These results show that the proposed spike-ripple detector performs well in this instance, and tends not to detect this sharp artifact.

In the third simulation scenario, the data consist of pink noise activity interspersed with spike events. These spike events were constructed to match the data from Patient E (see Table 1), and extend well above the simulated pink noise activity (Fig. 2c (i)). We note that the simulated data consist only of spike events – which appear at a rate of 1 Hz – but that these simulated data lack ripples. Applying the spike-ripple detector to 100 instances of these simulated data (each of duration 10 min, with 2035 Hz sampling rate) we find an average false positive rate between approximately 0.1 Hz and 0.0001 Hz, depending on the choice of envelope threshold. Again, as the envelope threshold increases, the false positive rate decreases; at an envelope threshold of 0.85, the false positive

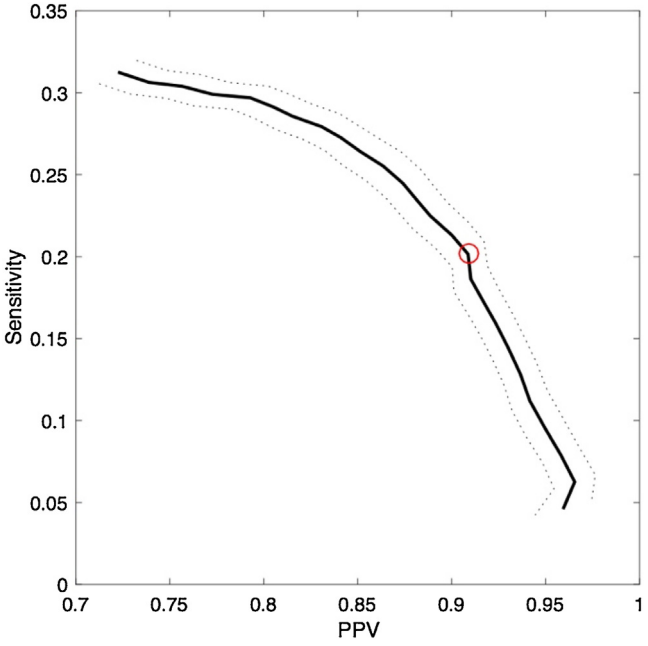

Fig. 3. Performance curve of the spike-ripple detector in simulation. The sensitivity versus the positive predictive value (PPV) at values of envelope threshold between 0.7 and 0.95. The thick black line indicates the mean value over 100 simulations, and the dotted curves indicate two standard errors of the mean. The red circle corresponds to an envelope threshold of 0.85. (For interpretation of the references to colour in this figure legend, the reader is referred to the web version of this article.)

rate is low (0.0055 Hz), and much lower than the 1 Hz rate of spike events. We conclude from these simulation results that the detector performs as expected, and tends not to detect spike events that lack ripples.

In the fourth simulation scenario, the data consist of pink noise activity interspersed with spike events in which each includes a ripple (see Methods). Visual inspection of the example trace in Fig. 2d (i) suggests the appearance of a low amplitude ripple event that begins on the rising phase of the spike, before the maximum value, although the ripple event is difficult to detect through visual inspection alone. Applying the spike-ripple detector to 100 instances of these simulated data (each of duration 10 min, with 2035 Hz sampling rate), we compute two quantities – the sensitivity and positive predictive value – over a range of envelope thresholds (Fig. 2d (ii)). We find that the average sensitivity varies between 0 and 0.4; at an envelope threshold of 0.85, the average sensitivity is 0.20. Although the method fails to detect every spike-ripple event (if it did, the sensitivity would be 1), we note that the spike-ripple detection rate (0.20 Hz at an envelope threshold of 0.85) is much higher than in the other simulation scenarios. Moreover, the positive predictive value is near 1 for all choices of envelope threshold (*i.e.*, fewer than 1% of the detections are false positives). We conclude from these results that the spike-ripple detector performs well in this case, which consists of true spike-ripple events.

In the last simulation, we again consider pink noise activity interspersed with spike events, here with a subset (1/3) of these spikes also possessing a ripple. We apply the spike-ripple detector to 100 instances of these simulated data (each of duration 10 minutes, with 2035 Hz sampling rate), and vary a parameter of the detector: the envelope threshold. We vary the envelope threshold between values of 0.7 and 0.95, and compute the positive predictive value and sensitivity of the spike-ripple detector (see Methods). We display the average of these two measures over the 100 instances of the simulated data as a performance curve (Fig. 3). As the envelope threshold increases, the positive predictive value increases and the sensitivity decreases. We note that, for all choices of envelope threshold, the sensitivity is less than 0.35 while the positive predictive value exceeds 0.7. One reason for the relatively low sensitivity and high positive predictive value is the number of features required of the candidate spike-ripple events (see Fig. 1). By employing numerous restrictions, we eliminate many candidate ripple events identified in Step 1 of the detector, which makes the detector less sensitive, but identifies candidate spike-ripple events that are more likely to be validated, so that the positive-predictive value is high. Although this approach will not detect all spike-ripple events, the time required for manual validation of candidate spike-ripple events is greatly reduced. Such a reduction is important when evaluating many electrodes recorded for long durations. In what follows, we fix the envelope threshold at 0.85 (red circle in Fig. 3). Here, we find in simulation that the sensitivity is 0.20 and the positive predictive values is 0.90; beyond this point the sensitivity rapidly decreases (Fig. 3). We note that increasing the amplitude of the ripple increases both the sensitivity and positive predictive value of the detector. However, we fix the ripple amplitude to 1/20 the spike amplitude, consistent with the spike-ripple events observed in the EEG from the patients considered here.

Combined, these results suggest that the proposed spike-ripple detector performs well in simulation. The false positive rate is low, and the positive predictive value is high. While the method fails to detect every spike-ripple event in the last two simulation scenarios (*i.e.*, the sensitivity is less than 0.35) the candidate events identified are predominantly true spike-ripple occurrences. In what follows, we fix the envelope threshold at 0.85; at this value, we find a low false detection rate, and a balance between the positive predictive value and sensitivity. We note that lower values of the envelope threshold result in higher false detection rates (Fig. 2b and c), while higher values of the envelope threshold reduce sensitivity (Fig. 3).

3.2. Analysis of scalp EEG data from ten patients

The simulations illustrate detector performance in different scenarios. However, no simulation can accurately capture all aspects of *in vivo* spike-ripple EEG activity. Therefore, we examine detector performance on EEG data collected from ten patients. Visual analysis of the EEG data from these patients reveals variability in the number of spikes detected in 10 min of data (maximum 234, minimum 0, mean 68; Table 1).

We perform two methods to detect ripples in these data. The first consists of visual inspection of the EEG at each spike, as implemented in (van Klink et al., 2016) and consistent with other studies (Kobayashi et al., 2010; Andrade-Valenca et al., 2011). The visualization consists of three items in the ±300 ms interval around the spike: (1) the unfiltered EEG data, (2) the high-pass filtered EEG data (>80 Hz), and (3) the spectrogram of the EEG data from 30 to 250 Hz. We note that, to compute the spectrogram, we use moving windows of duration 150 ms and step size of 5 ms. We multiply the data in each window by a Hanning taper, and then smooth the spectra computed at each time over ±25 ms. We also display the EEG data from all electrodes using an average reference. The purpose of this last display is to reject events that coincide with subtle muscle or movement artifacts affecting multiple channels. Visual identification of spikes and inspection for ripples for 10 min of data recorded at one electrode derivation took approximately 5 h per patient.

The second method we apply is the proposed spike-ripple detector. For example, for Patient A, this method identifies 35 candidate spike-ripple events, 22 of which were validated by visual inspection, as implemented in the first method described above. We show in Fig. 4 examples of detected and subsequently validated spike-ripple events. We note that, in each case the ripple activity is apparent through visual inspection of the unfiltered data (Fig. 4a). Inspection of the bandpass filtered EEG data (100–300 Hz; Fig. 4b,

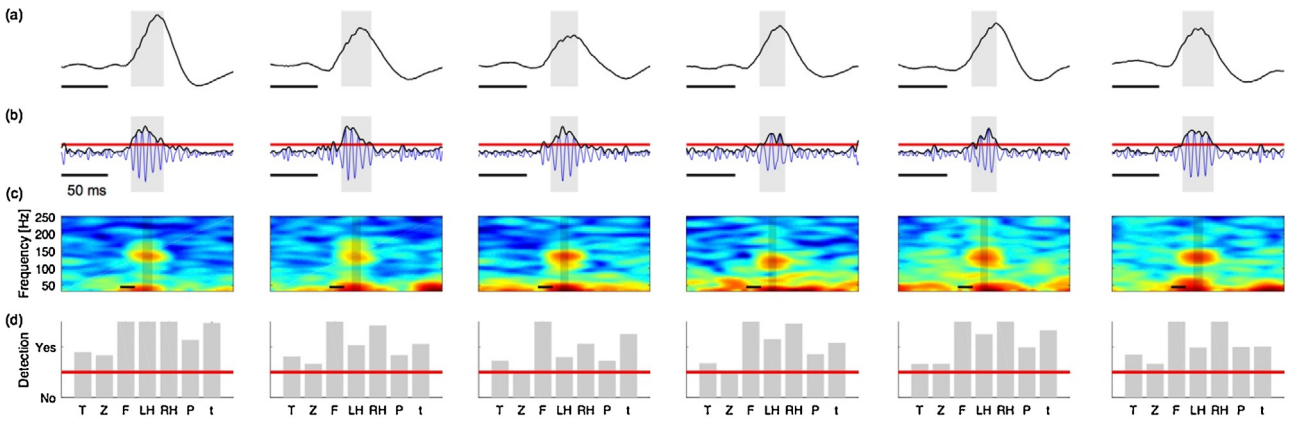

Fig. 4. Example spike-ripple detections (true positives) from EEG data.(For interpretation of the references to colour in this figure legend, the reader is referred to the web version of this article.)
(a) Unfiltered EEG data. The gray box indicates the time of the candidate spike-ripple event. A low amplitude ripple is visually evident on the ascending slope of each spike in the unprocessed data in each instance.
(b) Bandpass filtered EEG data (blue), amplitude envelope (black), and envelope threshold (red line).
(c) The spectrogram of EEG data in an interval surrounding the spike-ripple event (gray box). Power (in decibels) shown in color. A distinct high frequency "spectral island" is visually evident in each instance.
(d) Representation of seven features utilized in both stages of the spike-ripple detector. Each feature is normalized, so that values (gray bars) above the red line pass the detection threshold, while values below the red line do not. See text for definitions of each horizontal axis label.
In figures (a–c), scale bars indicate 50 ms.

blue) and corresponding amplitude envelope (Fig. 4b, black) shows that each ripple event exceeds the envelope threshold deduced from the entire duration of data (Fig. 4b, horizontal red line); as expected, during a ripple, the amplitude of the high frequency activity is larger than typically observed. Visualization of the spectrogram computed for the unfiltered data reveals power at low frequencies (near 30 Hz) and an isolated island of power at high frequencies during the time of each ripple event (Fig. 4c); we note that the appearance of distinct "spectral islands" is a component of our visual inspection to validate the detected events, but is not an explicit component of the detection algorithm. Finally, we show the relative values of the seven features that define the spike-ripple detector: (T) the duration of the ripple event must exceed 20 ms; (Z) the ripple event must possess at least 3 zero-crossings; (F) the Fano factor of the inter-crossing intervals must be less than 1; (LH,RH,P) the ripple must co-occur with a large voltage peak (P) that greatly exceeds the voltage values preceding (LH) and following (RH) the peak; and, (t) the ripple onset must precede the large voltage peak. We represent the relative values of these features as bars in Fig. 4d; for an event to register as a detection, all seven features must pass a threshold test (red line in Fig. 4d). For these detected and validated spike-ripple events, all seven measures do exceed the threshold tests. Running the spike-ripple detector and visual verification of all identified spike-ripple events detected in 10 min of data recorded at one electrode derivation took approximately 1–3 min per patient.

We show in Fig. 5 examples of true negative spike-ripple detections, which here consist of spikes without ripples. We note that visual inspection of the unfiltered EEG data does not identify ripples at these discharges (Fig. 5a). In most cases, the amplitude envelope of the high frequency activity fails to cross the envelope threshold (Fig. 5b). For the instances in which the amplitude envelope crosses the envelope threshold, the duration of this crossing is brief (less than 20 ms) and, for this reason, additional detection features are not estimated (Fig. 5d). Finally, visual inspection of the spectrogram does not suggest the presence of isolated islands of spectral power (Fig. 5c). These examples of spikes without ripples are not detected by the spike-ripple detector, as expected.

Applying the semi-automated spike-ripple detector to all ten patients, we detect and validate spikes (Table 1, third column) consistent with the results of standard visual analysis of the spikes (Table 1, second column). We note that more spike-ripple events were detected by visual analysis than using the spike-ripple detector. In this way, visual analysis may offer greater sensitivity at the cost of increased analysis time; we note that visual analysis begins with manual inspection of the EEG data to identify each occurrence of a spike. The spike-ripple detector requires no manual visual inspection until the final step of validation of candidate spike-ripple events. Such visual analysis may be particularly important when the number of spike-ripple events is small, as for Patient D. The false positive rate is low (for patients with 1 or more candidate spike-ripple detections, mean 0.023 Hz, minimum 0.007, maximum 0.05; Table 1, 4th column). For those patients in which more than one spike-ripple event was identified through visual inspection (Patients A–C), the method tends to detect spike-ripple events with high sensitivity (values of 0.30, 0.97, and 0.82; Table 1, 5th column), and a majority of the detections are validated (positive predictive values of 0.63, 0.68, and 0.33; Table 1; 6th column).

The method proposed here to detect spike-ripple events is semi-automated; candidate spike-ripple events detected by the method are subsequently validated by visual inspection. Here we find that, of the 190 candidate spike-ripple events detected, 94 were validated by visual inspection (Table 1). Because validation of the candidate events requires the subjective judgment of ripple quality by an expert reviewer, it is important to establish the repeatability of this validation. To account for this potential confound and assess the repeatability (or test-retest reliability) of each validation, we apply the following procedure. We note that this procedure is not part of the algorithm, but implemented here to explore the reliability of the visual inspection. First, we aggregate all 190 candidate spike-ripple detections from all patients. These candidate detections include both validated spike-ripple events, and rejected spike-ripple events (*e.g.*, spikes without ripples, or artifacts). We then choose at random (without replacement) a candidate spike-ripple event from this aggregate collection and visualize this event for validation. We perform this random selection of a candidate spike-ripple event until all 190 events are validated. We then repeat this entire procedure, choosing another random presentation of the 190 events. Upon completion, the expert reviewer has classified each candidate spike-ripple event twice, without knowledge of the patient from which the candidate event was drawn. We find

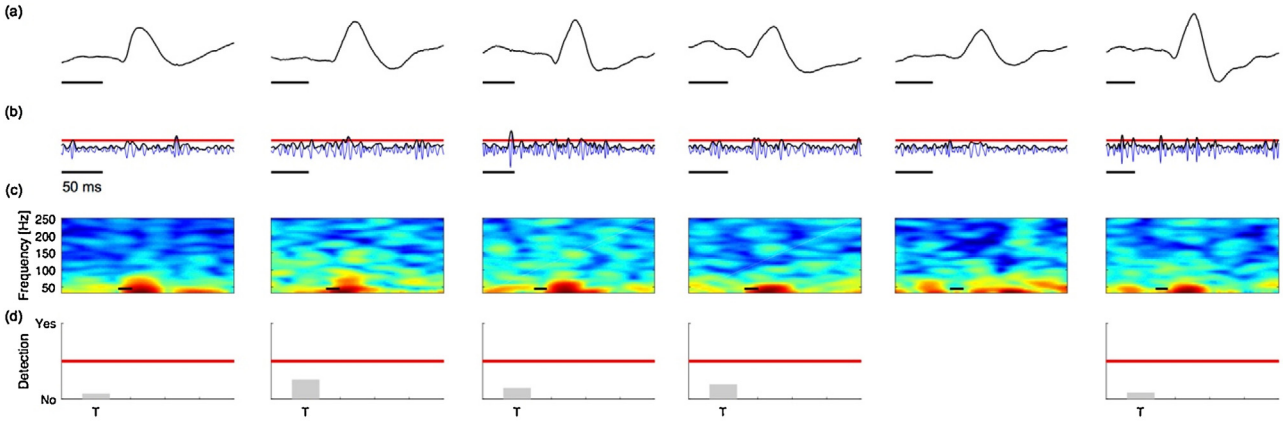

Fig. 5. Example spikes without ripples (true negatives) from the EEG data. (a) The unfiltered EEG data; (b) the bandpass filtered EEG data (blue), amplitude envelope (black) and envelope threshold (red); and, (c) the spectrogram of the EEG data. (d) Representation of features utilized in the spike-ripple detector. In figures (a–c), scale bars indicate 50 ms. See Fig. 4 caption for more details. (For interpretation of the references to colour in this figure legend, the reader is referred to the web version of this article.)

high intra-rater agreement; the observed proportional agreement is 0.96 and the kappa statistic is 0.92. These results suggest that the bias introduced by the subjective visual inspection of the candidate spike-ripple events is low, and that the repeatability of the procedure is high.

3.3. Different data quality and recording parameters produce qualitatively consistent results

For the results in Table 1, we analyzed high density EEG recordings during non-REM sleep with 65–71 electrodes (mean 69) per subject, at a sampling rate of 2035 Hz, with a common average reference. To evaluate the impact of changes in these data collection parameters, we consider several alternatives here.

The choice of electrode density and montage is an important issue in the analysis of EEG data (Nunez and Srinivasan, 2005; Chu et al., 2014; Lepage et al., 2014). To explore the impact of electrode density and montage choice on the proposed detection method, we consider three alterative scenarios: (1) a bipolar montage applied to a high-density recording, (2) a bipolar montage applied to a 10–20 low-density recording routinely used in the clinical setting, and (3) a common average reference applied to a low-density electrode configuration.

We perform these analyses on the two patients with the highest number of visually detected spikes in the active epilepsy and controlled epilepsy groups (Patient A and Patient E, respectively). The results from the four different scenarios are qualitatively consistent (Table 2, columns 1–4); in particular, we note that the number of validated spike-ripple events is non-zero in Patient A, and zero in Patient E, as expected. We also note that the high-density electrode configurations detect more validated spike-ripple events, and produce fewer rejected spike-ripple events, than the corresponding low-density electrode configurations.

Of the 94 validated spike-ripple detections in our dataset, the ripple frequency ranged from 104 to 235 Hz (mean 142 Hz). To evaluate the minimum sampling rate required to reliably detect spike-ripples in these data, we test two lower sampling rates (corresponding to integer decimations of our initial sampling rate) consistent with those used in clinical settings: 254.4 Hz and 508.7 Hz, on the above two patients. In Patients A and E, we find that the detector identifies 39 candidate spike-ripple events at 254.4 Hz performed, but none of these were validated on visual analysis (Table 2, column 5). At 508.7 Hz sampling rate, the detector identifies 33 candidate spike-ripple events in Patient A, of which 16 are validated upon visual analysis, while in Patient E, the detector identifies18 candidate spike-ripple events, none of which are validated on visual analysis (Table 2, column 3). These results support the intuitive notion that detection of spike-ripple events becomes more reliable when these events are better resolved at higher sampling rates.

In addition, to evaluate the impact of increased muscle and movement artifacts on detector performance, we evaluate 10 min of continuous wake EEG activity from these two representative subjects (Table 2, column 7). Again, we find qualitatively consistent results as during sleep; the number of validated spike-ripple events is non-zero in Patient A, and zero in Patient E, as expected. These results add confidence that the proposed method performs consistently across a variety of electrode densities, referencing montages, sampling rates, and states of consciousness.

4. Discussion

Brief high frequency oscillations observed in human brain voltage activity are incompletely understood. Experimental observations in animal models suggest that these fast oscillations reflect rapid inhibitory postsynaptic potentials (IPSPs) on the somata of pyramidal cells during simultaneous excitation of the pyramidal cells and surrounding interneurons (Bragin et al., 1999). An alternative mechanism – axo-axonal gap junctions between pyramidal cells – has also been proposed to support ripple band activity (Traub et al., 2001; Simon et al., 2014). Ripple oscillations have been observed in healthy tissue and may reflect normal physiological processes that contribute to the synaptic remodeling that underlies information processing, memory transference and consolidation (Buzsaki and Lopes da Silva, 2012). Conversely, when coupled to pathologic interictal epileptiform discharges, ripple events may reflect a malignant hijacking of these powerful processes of neuronal synchronization and thereby both reflect and contribute to the underlying disease (Bragin et al., 1999).

Robust coupling between sharp wave discharges and ripples has been observed in animal and human invasive recordings (Ylinen et al., 1995; Buzsaki and Lopes da Silva, 2012) and in scalp EEG (Kobayashi et al., 2010; Von Ellenrieder et al., 2016; Jacobs et al., 2009; van Klink et al., 2016). Although it is compelling to compare scalp spike-ripple events to intracranial spike-ripple events, these signals appear to behave differently and may represent altered propagation of shared generators (von Ellenrieder et al., 2014) or different underlying mechanisms (Worrell and Gotman, 2011). Although irregular oscillations have been observed in ripples recorded intracranially (Menendez de la Prida et al., 2015), we limit the ripple oscillations to small Fano factors to match pre-

Table 2
The spike-ripple detector performs well in different recording scenarios. In all columns, the values indicate the number of spike-ripples identified by the proposed detector (in parentheses) and validated through visual inspection. First column, high-density common average reference (CAR) montage, identical to the third column of Table 1. Second column, low-density CAR montage. Third and fourth columns, bipolar montages with high-density and low-density electrode configurations, respectively. Fifth and sixth columns, high-density CAR montage with data sampled at 254.4 Hz and 508.7 Hz, respectively. Seventh column, high-density CAR montage with data recorded during wake.

	High-density CAR, Wake	Low-density CAR	High-density bipolar	Low-density bipolar	High-density CAR, 254.4 Hz	High-density CAR, 508.7 Hz	High-density CAR, Sleep
Patient A	22 (35)	8 (23)	53 (74)	39 (77)	0 (14)	16 (33)	24 (41)
Patient E	0 (16)	0 (20)	0 (1)	0 (13)	0 (25)	0 (18)	0 (0)

vious descriptions of spike-ripple oscillations as sinusoidal activity in scalp EEG (Von Ellenrieder et al., 2012) and minimize false detection, as irregular oscillations have been noted to reflect artifact (Andrade-Valenca et al., 2011). We also required that the onset of the ripple precede the large voltage peak as this was observed in our data and consistent with the examples of scalp spike-ripples shown in prior publications (Kobayashi et al., 2010; Von Ellenrieder et al., 2012; van Klink et al., 2016). The mechanisms of these empirical observations remain unclear. Paroxysmal depolarizing shifts (PDS) lasting approximately 100–500 ms have been observed to coincide with interictal discharges and are thought to directly reflect summated excitatory postsynaptic potentials (Ayala et al., 1973). These depolarizing shifts are thought to be circumscribed by an "inhibitory surround" that, in some spike events, may generate the pattern of inhibitory potentials that create ripple activity.

Detection of ripple events during interictal spikes raises some methodological issues. Scalp EEG spike ripples have been observed to occur between 93 and 235 Hz (Kobayashi et al., 2010; van Klink et al., 2016). If a low pass filter is applied during data collection or analysis, it should be above this range. Similarly, the sampling rate must be sufficient to reliably expose the signals of interest; the minimum sampling rate reported in the literature for visual analysis of spike ripples is 500 Hz (Kobayashi et al., 2010), consistent with the performance of our detector, as most spike-ripples occur <150 Hz. We find that variations in montage choice, electrode density, and state of consciousness do not qualitatively impact detector performance; however, the detector had the best performance when high-density recordings with a high sampling rate were used. We also note that high pass filtering of EEG data with rapid voltage changes, such as seen in epileptiform spikes, can introduce ringing artifacts that appear as ripples or fast oscillations (Bénar et al., 2010; Menendez de la Prida et al., 2015; Kramer et al., 2008). We thus applied several conservative steps to mitigate this possible confound. First, in our manual validation of candidate spike-ripple events, we required a fast oscillation be visible on the unfiltered data. Second, we tested our detector in simulations that included large, rapid changes in voltage, such as triangle waves as well as simulated epileptiform discharges interpolated from empirical data with and without superimposed oscillatory ripple events. Finally, we tested our detector using empirical human data where ripples were and were not observed. In the clinical data and in each of the simulated scenarios, the detector performs with high positive predictive value and low false detection rate.

By relying on the presence of interictal spikes, the proposed method is limited to the sensitivity of interictal spikes for epileptiform processes. In longer recordings, interictal discharges are reported in 81% of people with epilepsy, and sensitivity is further increased using provocative procedures and capturing sleep (Walczak et al., 1993; Pillai and Sperling, 2006). Some of the missed cases are due to the limitation of the scalp EEG in accessing deep or small epileptogenic regions; ripple identification on scalp EEG would suffer the same challenge and is thus not expected to improve substantially with more thorough data review. However, a previous study showed that 63% of manually identified scalp high frequency oscillations identified were concurrent with spikes (Jacobs et al., 2009). A less specific semi-automated fast oscillation detection method that did not rely on spikes for fast oscillation detection reported that 50–70% of fast oscillations occur at the same time as a spike (Von Ellenrieder et al., 2012). Thus, while our method has been developed to detect the majority of ripple events, those events that occur between spikes will be missed. Reducing the number of automated detections makes the subsequent validation through visual inspection tractable for large data sets. Ideally, this reduction would occur by reducing the false positive rate while preserving or improving the positive predictive value.

The proposed method still requires the manual validation of spike-ripple events, a subjective procedure which may introduce bias and reduce reliability. To test for this here, we de-identified and scrambled the EEG data prior to expert review, and found high intra-rater reliability. This result suggests that the candidate spike-ripple events detected by the proposed method are easily validated or refuted. We note that this procedure is only tractable when the number of candidate events is small, as is the case here when only spikes that occur with ripples are detected. Future work will focus on further automating these techniques to eliminate subjective bias and labor introduced by manual review, and applying this approach to a larger patient population to further test the utility of this method.

Here we introduce a semi-automated spike-ripple detector with the goal of facilitating efficient exploration of large datasets including high-density electrode sampling as well as longer duration recordings. Evaluation of larger datasets is essential to further investigate the sensitivity and specificity of this biomarker to predict seizure risk in patients with spikes. Furthermore, rapid identification and characterization of pathological ripples in non-invasive EEG data facilitates exploration of the relationship between these events and clinical consequences in a wide variety of clinical scenarios, including how they relate to epileptogenesis and other disease related morbidities often present in epilepsy, such as sleep, attentional, behavioral, and memory difficulties (Worrell and Gotman, 2011; Engel et al., 2009).

Acknowledgements

Funding: This work was supported by the National Institutes of Health [Award Numbers P41RR14075, 1S10RR031599]; NINDS [Award Numbers K23NS092923, 5R01NS069696, R01NS095369, and R01NS072023]; the National Science Foundation DMS [Award #1451384], CBET [Award #1141995]]. We thank Wenting Xie, Rebecca Weiss, Erin Ross, Emily Thorn, and Lauren Ostrowski for assistance with clinical subject recruitment and data collection.

References

Andrade-Valença, L., Mari, F., Jacobs, J., Zijlmans, M., Olivier, A., Gotman, J., Dubeau, F., 2012. Interictal high frequency oscillations (HFOs) in patients with focal epilepsy and normal MRI. Clin. Neurophysiol. 123 (January (1)), 100–105, http://dx.doi.org/10.1016/j.clinph.2011.06.004, Epub 2011 July 2.

Andrade-Valenca, L.P., Dubeau, F., Mari, F., Zelmann, R., Gotman, J., 2011. Interictal scalp fast oscillations as a marker of the seizure onset zone. Neurology 77, 524–531.

Axmacher, N., Elger, C.E., Fell, J., 2008. Ripples in the medial temporal lobe are relevant for human memory consolidation. Brain 131 (July (Pt. 7)), 1806–1817, http://dx.doi.org/10.1093/brain/awn103, Epub 2008 May 24.
Ayala, G.F., Dichter, M., Gumnit, R.J., Matsumoto, H., Spencer, W.A., 1973. Genesis of epileptic interictal spikes, new knowledge of cortical feedback systems suggests a neurophysiological explanation of brief paroxysms. Brain Res. 52, 1–17.
Bénar, C.G., Chauviere, L., Bartolomei, F., Wendling, F., 2010. Pitfalls of high-pass filtering for detecting epileptic oscillations: a technical note on false ripples. Clin. Neurophysiol. 121 (3), 301–310.
Bennett, D.R., 1967. Spike-wave complexes in normal flying personnel. Aerosp. Med. 38, 1276–1282, Electroencephalogram epileptiform abnormalities in candidates for aircrew training.
Blanco, J.A., Stead, M., Krieger, A., et al., 2010. Unsupervised classification of high-frequency oscillations in human neocortical epilepsy and control patients. J. Neurophysiol. 104, 2900–2912.
Bragin, A., Engel, J., Wilson, C.L., Fried, I., Buzsaki, G., 1999. High-Frequency oscillations in human brain. Hippocampus 9, 137–142.
Buzsaki, G., Lopes da Silva, F., 2012. High frequency oscillations in the intact brain. Prog. Neurobiol. 98, 241–249.
Chu, C.J., Leahy, J., Pathmanathan, J., Kramer, M.A., Cash, S.S., 2014. The maturation of cortical sleep rhythms and networks over early development. Clin. Neurophys. 125, 1360–1370.
Crépon, B., Navarro, V., Hasboun, D., Clemenceau, S., Martinerie, J., Baulac, M., et al., 2010. Mapping interictal oscillations greater than 200 Hz recorded with intracranial macroelectrodes in human epilepsy. Brain: J. Neurol. 133 (Pt.1), 33–45.
Eeg-Olofsson, O., Petersen, I., Sellden, U., 1971. The development of the electroencephalogram in normal children from the age of 1 through 15 years: paroxysmal activity. Neuropadiatrie 2, 375–404.
Efron, B., Gong, G., 1983. A leisurely look at the bootstrap the jackknife, and cross-validation. Am. Stat. 37 (1), 36–48.
Engel Jr., J., Bragin, A., Staba, R., Mody, I., 2009. High-frequency oscillations: what is normal and what is not? Epilepsia 50, 598–604.
Gardner, A.B., Worrell, G.A., Marsh, E., Dlugos, D., Litt, B., 2007. Human and automated detection of highfrequency oscillations in clinical intracranial EEG recordings. Clin. Neurophysiol. 118, 1134–1143.
Gregory, R.P., Oates, T., Merry, R.T., 1993. Electroencephalogram epileptiform abnormalities in candidates for aircrew training. Electroencephalogr. Clin. Neurophysiol. 86 (1), 75.
He, B.J., Zempel, J.M., Snyder, A.Z., Raichle, M.E., 2010. The temporal structures and functional significance of scale-free brain activity? Neuron 66 (3), 353–369.
Inoue, T., Kobayashi, K., Oka, M., Yoshinaga, H., Ohtsuka, Y., 2008. Spectral characteristics of EEG gamma rhythms associated with epileptic spasms. Brain Dev. 30 (May (5)), 321–328, Epub 2008 Feb 20.
Jacobs, J., Zelmann, R., Jirsch, J., Chander, R., Dubeau, C.E., Gotman, J., 2009. High frequency oscillations (80–500 Hz) in the preictal period in patients withfocal seizures. Epilepsia 50 (July (7)), 1780–1792.
Jacobs, J., Zijlmans, M., Zelmann, R., et al., 2010. Value of electrical stimulation and high frequency oscillations (80–500 Hz) in identifying epileptogenic areas during intracranial EEG recordings. Epilepsia 51, 573–582.
Jirsch, J.D., Urrestarazu, E., LeVan, P., Olivier, A., Dubeau, F., Gotman, J., 2006. High-frequency oscillations during human focal seizures. Brain 129, 1593–1608.
Kobayashi, K., Oka, M., Akiyama, T., Inoue, T., Abiru, K., Ogino, T., Yoshinaga, H., Ohtsuka, Y., Oka, E., 2004. Very fast rhythmic activity on scalp EEG associated with epileptic spasms. Epilepsia 45 (May (5)), 488–496.
Kobayashi, K., Watanabe, Y., Inoue, T., Oka, M., Yoshinaga, H., Ohtsuka, Y., 2010. Scalp-recorded high-frequency oscillations in childhood sleep-induced electrical status epilepticus. Epilepsia 51, 2190–2194.
Kramer, M.A., Tort, A.B.L., Kopell, N.J., 2008. Sharp edge artifacts and spurious coupling in EEG frequency comodulation measures. J. Neurosci. Methods 170 (2), 352–357.
Lepage, K.Q., Kramer, M.A., Chu, C.J., 2014. A statistically robust EEG re-referencing procedure to mitigate reference effect. J. Neurosci. Methods 235, 101–116.
Menendez de la Prida, L., Staba, R.J., Dian, J.A., 2015. Conundrums of high-frequency oscillations (80–800 Hz) in the epileptic brain? J. Clin. Neurophysiol. 32 (3), 207–219.
Nunez, P.L., Srinivasan, R., 2005. Electric Fields of the Brain: the Neurophysics of EEG, 2nd ed. Oxford UP, New York.
Pillai, J., Sperling, M.R., 2006. Interictal EEG and diagnosis of epilepsy. Epilepsia 47 (Suppl.1), 14–22.
Simon, A., Traub, R.D., Vladimirov, N., Jenkins, A., Nicholson, C., Whittaker, R.G., et al., 2014. Gap junction networks can generate both ripple-like and fast ripple-like oscillations. Eur. J. Neurosci. 39 (1), 46–60.
Staba, R.J., Wilson, C.L., Bragin, A., Jhung, D., Fried, I., Engel Jr., J., 2004. High-frequency oscillations recorded in human medial temporal lobe during sleep. Ann. Neurol. 56 (July (1)), 108–115.
Staba, R.J., Frighetto, L., Behnke, E.J., Mathern, G.W., Fields, T., Bragin, A., Ogren, J., Fried, I., Wilson, C.L., Engel Jr., J., 2007. Increased fast ripple to ripple ratios correlate with reduced hippocampal volumes and neuron loss in temporal lobe epilepsy patients. Epilepsia 48, 2130–2138.
Tao, J.X., Baldwin, M., Hawes-Ebersole, S., Ebersole, J.S., 2007. Cortical substrates of scalp EEG epileptiform discharges. J. Clin. Neurophysiol. 24, 96–100.
Traub, R.D., Jefferys, J.G., 1994. Simulations of epileptiform activity in the hippocampal CA3 region in vitro. Hippocampus 4 (June (3)), 281–285.
Traub, R.D., Borck, C., Colling, S.B., Jefferys, J.G., 1996. On the structure of ictal events in vitro. Epilepsia 37 (September (9)), 879–891.
Traub, R.D., Whittington, M.A., Buhl, E.H., LeBeau, F.E., Bibbig, A., Boyd, S., et al., 2001. A possible role for gap junctions in generation of very fast EEG oscillations preceding the onset of and perhaps initiating, seizures. Epilepsia 42 (2), 153–170.
Urrestarazu, E., Chander, R., Dubeau, F., Gotman, J., 2007. Interictal high-frequency oscillations (100–500 Hz) in the intracerebral EEG of epileptic patients. Brain 130 (September (Pt. 9)), 2354–2366.
Von Ellenrieder, N., Andrade-Valenca, L.P., Dubeau, F., Gotman, J., 2012. Automatic detection of fast oscillations (40–200 Hz) in scalp EEG recordings. Clin. Neuorphysiol. 123 (4), 670–680.
Von Ellenrieder, N.V., Frauscher, B., Dubeau, F., Gotman, J., 2016. Interaction with slow waves during sleep improves discrimination of physiologic and pathologic high-frequency oscillations (80–500 Hz). Epilepsia 57 (6), 869–878.
van Klink, N.E., van't Klooster, M.A., Leijten, F.S., Jacobs, J., Braun, K.P., Zijlmans, M., 2016. Ripples on rolandic spikes: a marker of epilepsy severity. Epilepsia. 57 (July (7)), 1179–1189, http://dx.doi.org/10.1111/epi.13423, Epub 2016 Jun 8.
von Ellenrieder, N., Beltrachini, L., Perucca, P., 2014. Gotman J.Size of cortical generators of epileptic interictal events and visibility on scalp EEG. Neuroimage 94, 47–54.
Walczak, T.S., Scheuer, M.L., Resor, S., et al., 1993. Prevalence and features of epilepsy without interictal epileptiform discharges. Neurology 43 (Suppl), 287–288.
Worrell, G., Gotman, J., 2011. High-frequency oscillations and other electrophysiological biomarkers or epilepsy: clinical studies. Biomark. Med. 5, 557–566.
Worrell, G.A., Parish, L., Cranstoun, S.D., Jonas, R., Baltuch, G., Litt, B., 2004. High-frequency oscillations and seizure generation in neocortical epilepsy. Brain 127, 1496–1506.
Worrell, G.A., Gardner, A.B., Stead, S.M., et al., 2008. High-frequency oscillations in human temporal lobe: simultaneous microwire and clinical macroelectrode recordings. Brain 131, 928–937.
Wu, J.Y., Sankar, R., Lerner, J.T., Matsumoto, J.H., Vinters, H.V., Mathern, G.W., 2010. Removing interictal fast ripples on electrocorticography linked with seizure freedom in children. Neurology 75, 1686–1694.
Ylinen, A., Bragin, A., Nadazdy, Z., Jando, G., Szabo, I., Sik, A., Buzsaíki, G., 1995. Sharp wave-associated high-frequency oscillation (200 Hz) in the intact hippocampus: network and intracellular mechanisms. J. Neurosci. 15, 30–46.
Zelmann, R., Zijlmans, M., Jacobs, J., Châtillon, C.-E., Gotman, J., 2009. Improving the identification of high frequency oscillations. Clin. Neurophysiol. 120 (8), 1457–1464, http://dx.doi.org/10.1016/j.clinph.2009.05.029.
Zelmann, R., Mari, F., Jacobs, J., Zijlmans, M., Dubeau, F., Gotman, J., 2012. A comparison between detectors of high frequency oscillations. Clin. Neurophysiol.
Zijlmans, M., Jacobs, J., Zelmann, R., Dubeau, F., Gotman, J., 2009. High-frequency oscillations mirror disease activity in patients with epilepsy. Neurology 72, 979–986.